

Topological charge density wave in monolayer NbSe₂

Wei-Chi Chiu,^{1,*} Sougata Mardanya,² Robert Markiewicz,¹
Jouko Nieminen,^{3,1} Bahadur Singh,⁴ Tugrul Hakioglu,^{5,1} Amit
Agarwal,⁶ Tay-Rong Chang,^{2,7,8} Hsin Lin,⁹ and Arun Bansil^{1,†}

¹*Department of Physics, Northeastern University, Boston, MA 02115, USA*

²*Department of Physics, National Cheng Kung University, Tainan 70101, Taiwan*

³*Computational Physics Laboratory,*

Tampere University, Tampere 33014, Finland

⁴*Department of Condensed Matter Physics and Materials Science,
Tata Institute of Fundamental Research, Colaba, Mumbai 400005, India*

⁵*Energy Institute and Department of Physics,*

Istanbul Technical University, Maslak 34469, Istanbul, Turkey

⁶*Department of Physics, Indian Institute of Technology Kanpur, Kanpur 208016, India*

⁷*Center for Quantum Frontiers of Research and Technology (QFort), Tainan 701, Taiwan*

⁸*Physics Division, National Center for Theoretical Sciences,*

National Taiwan University, Taipei, Taiwan

⁹*Institute of Physics, Academia Sinica, Taipei 11529, Taiwan*

(Dated: May 5, 2021)

ABSTRACT

Despite the progress made in successful prediction of many classes of weakly-correlated topological materials, it is not clear how a topological order can emerge from interacting orders and whether or not a charge ordered topological state can exist in a two-dimensional (2D) material. Here, through first-principles modeling and analysis, we identify a 2×2 charge density wave (CDW) phase in monolayer $2H$ -NbSe₂ that harbors coexisting quantum spin Hall (QSH) insulator, topological crystalline insulator (TCI) and topological nodal line (TNL) semimetal states. The topology in monolayer NbSe₂ is driven by the formation of the CDW and the associated symmetry-breaking periodic lattice distortions and not via a pre-existing topology. Our finding of an emergent triple-topological state in monolayer $2H$ -NbSe₂ will offer novel possibilities for exploring connections between different topologies and a unique materials platform for controllable CDW-induced topological states for potential applications in quantum electronics and spintronics and Majorana-based quantum computing.

INTRODUCTION

A new frontier in condensed matter physics concerns the study of emergent topological phases in correlated materials [1, 2]. Recent proposals, which have focused on realizing a topological charge ordered (TCO) state in materials [3–6] start by assuming a pre-existing topological order before introducing the charge density wave (CDW) transition. It remains unclear how a topological state could emerge driven by the spontaneous symmetry breaking (SSB) involved in the formation of the CDW itself. Here, our first-principles modeling and analysis shows that a 2×2 CDW phase of a $2H$ -NbSe₂ monolayer film can support a complex topological phase with three co-existing topological states even though a pristine $2H$ -NbSe₂ film has a trivial band topology.

Since the discovery of the quantum spin Hall (QSH) insulator [7–9], or 2D topological insulator (TI), a variety of topological insulators and semimetals have been proposed in 2D materials such as topological crystalline insulators (TCI) [10, 11] and topological nodal line (TNL) semimetals [12, 13]. Both QSH insulators and TCI are novel quantum materials with insulating bulk states but conducting edge states that are topologically protected either by the time reversal symmetry (TRS) or the crystalline symmetries. It is also possible that the QSH and TCI can coexist in a 2D material preserving both time-reversal and mirror symmetries as, for example, in monolayer Na₃Bi [14]. The QSH state with its associated quantized Hall conductance without an external magnetic field was first observed in HgTe/CdTe quantum wells [15, 16]. It has also been predicted [17] and observed experimentally [18, 19] in monolayer transition metal dichalcogenide (TMD) film of WTe₂.

TMDs display a dazzling variety of correlated phases, including CDW [20, 21], superconductivity and magnetic orders [22]. In recent years, TMDs have become available as monolayers [23], which are extremely elastic, and can withstand large in-plane strains ($> 10\%$) [24] and provide an ideal playground for designing topological phases [18, 19, 25] and the manipulation of many-body ground states [26–29]. In particular, bulk $2H$ -NbSe₂ is one of the most extensively studied TMDs that exhibits both superconductivity ($T_c \sim 7.2$ K) [30] and a triangular (3Q) incommensurate CDW with $\sim 3a_0$ period in real space ($T_{CDW} \sim 33$ K) [31]. $2H$ -NbSe₂ has strongly layer-dependent properties [32], with monolayer $2H$ -NbSe₂ (also referred as the $1H$ structure [17]) hosting enhanced $3a_0$ period triangular (3Q) CDW order ($T_{CDW} \sim 145$ K) [33, 34] and weaker superconductivity ($T_c \sim 1.9$ K) [35, 36] which

may have an exotic Ising pairing [37, 38].

Scanning tunneling microscopy (STM) experiments find two unexpected CDW phases in monolayer $2H$ -NbSe₂ with applied in-plane biaxial tensile strain: one phase has a triangular (3Q) order with period $2a_0$ while the other is a unidirectional stripe (1Q) order with period $4a_0$ [39]. A similar unidirectional stripe phase with period $\sim 3.5a_0$ has been observed in bulk $2H$ -NbSe₂ [40], but there is no report of a bulk triangular (3Q) order with period $2a_0$. Experimentally, the heavily electron-doped monolayer NbSe₂ also hosts a 2×2 CDW order [41]. *Ab initio* calculations have established the modulated crystal structure of the triangular $3a_0$ [42–44] and stripe $4a_0$ [45] CDW phases of monolayer $2H$ -NbSe₂, but the crystal structure of the 2×2 CDW is not known. Due to the wide application of NbSe₂ [23, 46] and the important role of substrate strain in monolayer materials, it is crucial to understand the structural ground state and electronic properties of this phase.

In this article, we discuss *ab initio* calculations within the density functional theory (DFT) framework to establish the structure of the 2×2 triangular CDW in monolayer $2H$ -NbSe₂. We show that, by applying an in-plane biaxial tensile strain, the soft phonon mode of the unmodulated structure shifts from momentum $\mathbf{q}_{CDW} \sim 2/3 \Gamma M$ to $\mathbf{q}_{CDW} \sim \Gamma M$, which implies that the instability leads to a structural reconstruction related to a triangular period $2a_0$ charge order. We find two stable 2×2 CDW phases with slightly different energies, which are in the pattern of a breathing mode. Above a certain in-plane biaxial strain, the 2×2 phase becomes the ground state. Finally, we unveil the emergence of non-trivial time-reversal protected \mathbb{Z}_2 and mirror-protected \mathbb{Z} classes of topologies in the CDW phase, and show that the CDW phase of monolayer $2H$ -NbSe₂ hosts three co-existing topological states.

STRAIN-INDUCED INSTABILITIES

While bulk $2H$ -NbSe₂ is a van der Waals material with centrosymmetric space group $P6_3/mmc$ (No. 194) containing inversion symmetry, the monolayer $2H$ -NbSe₂ has a non-centrosymmetric $P\bar{6}m2$ (No. 187) space group with an additional out-of-plane mirror symmetry M_z but no inversion symmetry. Fig. 1a shows the top view of the hexagonal structure of monolayer NbSe₂, and the Nb layer, which acts as a mirror plane for the M_z , is sandwiched between two Se layers as shown in Fig. 1b. Each Nb atom sits inside a trigonal prismatic cell formed by six nearest-neighbor Se atoms as shown in Fig. 1c. Our calculations show

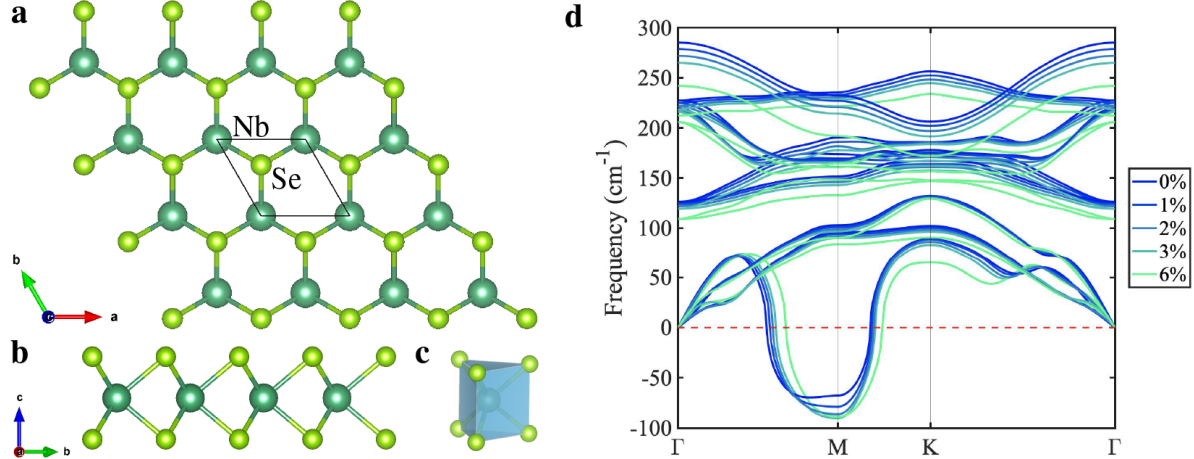


FIG. 1. **2H-NbSe₂ normal phase.** (a-c) Crystal structure of unmodulated monolayer 2H-NbSe₂. Nb and Se atoms are shown as dark green and light green spheres. **a**, Top view of the crystal structure. **b**, Side view of the crystal structure. **c**, The trigonal prismatic cell. **d**, The phonon spectrum of unmodulated monolayer 2H-NbSe₂ with different in-plane biaxial strain. The phonon spectrum for larger strain values up to 10% strain is presented in Supplementary Materials (SM) S.1.

that Nb atoms form a perfect hexagonal close-packed structure, with the shortest Nb-Nb separation $a_0 = 3.485 \text{ \AA}$.

The normal unmodulated phase of monolayer 2H-NbSe₂ is found to be unstable below the CDW critical temperature [33, 34] and it exhibits a prominent soft phonon mode around $\mathbf{q}_{CDW} \sim 2/3 \Gamma M$ in our calculations, indicating a strong structural instability to CDW formation with a 3×3 supercell, consistent with experiment [33, 34]. As shown in Fig. 1d and SM S.1., with increasing in-plane biaxial tensile strains, the soft phonon modes shift from $\mathbf{q}_{CDW} \sim 2/3 \Gamma M$ to $\mathbf{q}_{CDW} \sim \Gamma M$ which implies a structural instability with 2×2 CDW modulations. [21, 47] This dependence of the soft phonon mode on the applied strain indicates a strain-induced structural phase transition from 3×3 to 2×2 CDW phase. Furthermore, the 3×3 phase competes strongly with the 2×2 phase when the strain is around 0%-1% due to the relative flatness of the soft phonon mode between $2/3 \Gamma M$ and M point. The broad range of q -vectors which simultaneously soften is consistent with a phonon-entropy dominated transition [48]. We emphasize that while the strain applied in DFT calculations is not directly comparable to the strain applied in experiment ($\sim 0.15\%$), the DFT calculation

can still capture the tendency of structural reconstruction by calculating the ground state energy of each phase.

2×2 CDW BREATHING MODE

The crystal structure of monolayer $2H$ -NbSe₂ in the CDW state was obtained with multiple structural optimizations with a 2×2 supercell under different in-plane biaxial tensile strain varying from 0% to 10%. Before each optimization, small in-plane displacements preserving the C_3 symmetry were added to Nb atoms on the edge and at the center of the supercell (the triangular Nb trimer), leaving the Nb atoms at the corner of the supercell unchanged. Depending on the direction of the initial displacements, two different phases of CDW modulation emerge after all the atom positions are relaxed in the 2×2 supercell. With the extended 2×2 supercell as new unit cell, these two 2×2 CDW modulated structures have the same space group $P\bar{6}m2$ (No. 187) as the unmodulated structure in the 1×1 unit cell which reflects the nature of SSB in translational symmetry. The first Brillouin zone of the 2×2 supercell is accordingly folded from the 1×1 as shown in Fig. 2e. With the same space group, the Nb layer is still a mirror plane for M_z , and these two different phases can be characterized by the in-plane displacements of the Nb atomic layer, with concomitant displacements of Se atoms.

In analogy with the two known 3×3 phases (see SM S.3.) [43], we can label the two 2×2 CDW phases, shown in the insets of Fig. 2f, as 1+3-hollow (phase 1) and 1+3-filled (phase 2). The periodic lattice distortion (PLD) of phase 1 is shown in Fig. 2a (top view) and Fig. 2b (side view). Three Nb atoms on the hexagonal ring within the 2×2 unit cell are shifted inward to the center of the hexagonal ring, as in the breathing-in phase of a breathing mode, and form the hollow triangular Nb trimer with no Se atoms at the center. The six Se atoms on the hexagonal ring move (slightly) away from the center of the ring. All these Nb and Se atoms, which formed the hexagonal ring within the 2×2 unit cell, only have in-plane modulation vectors with no out-of-plane component. As shown in Fig. 2b, those Se with three Nb atoms moving away from them have the modulations purely out-of-plane toward the Nb layer.

As shown in Fig. 2c-d, the PLD of second phase is also dominated by the same three Nb atoms, but now moving outward from the center of the hexagonal ring, so that three Nb

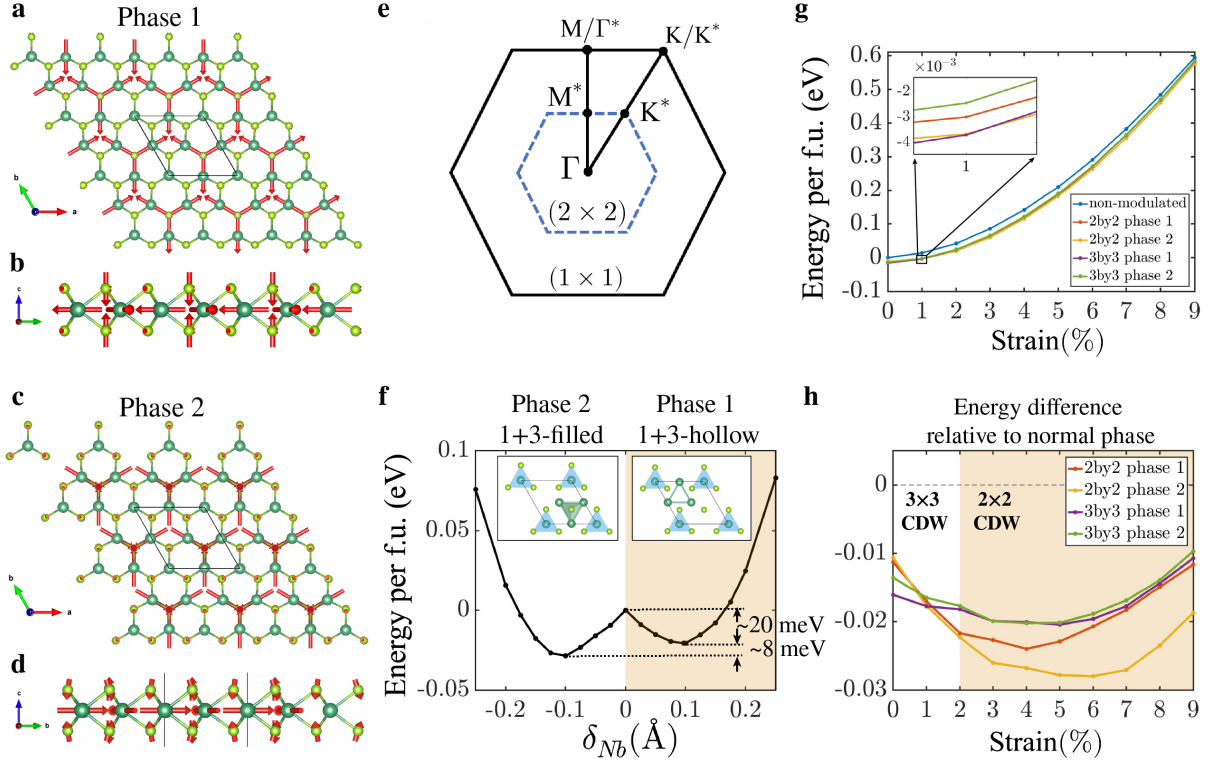


FIG. 2. 2×2 CDW breathing mode. (a-d) Crystal structure of two 2×2 CDW phases in monolayer $2H$ -NbSe₂. Nb and Se atoms are shown as dark green and light green spheres, respectively. The red arrows represent the modulation vectors of each atoms compared to the unmodulated structure. a/c, Top view of the crystal structure for the phase 1/phase 2. b/d, Side view of the crystal structure for the phase 1/phase 2. e, 2D first Brillouin zones (BZs) of the monolayer in the 1×1 normal phase (black solid lines) and the 2×2 CDW phase (blue dashed lines) with three high-symmetry points, Γ , M , and K . The high-symmetry points of the 2×2 BZ are marked with a star (*). f, The energy per formula unit (f.u.) of the 2×2 supercell under 6% strain as a function of Nb trimer distortion δ_{Nb} . The right/left inset shows the unit cell of phase 1/phase 2. The green lines represent the shortened length between two adjacent Nb-Nb atoms in the CDW phase. g, Total energy per f.u. of the normal phase, two 2×2 CDW phases and two 3×3 CDW phases as a function of strain. The zero point is set to the energy of unmodulated structure without strain. The inset in g shows the zoom-in region around 1% strain. h, The differences of total energy per f.u. relative to the energy of normal phase as a function of strain. The 2×2 CDW phase becomes the ground state when the strain is larger than 1%.

from different rings all move toward the Se atom at their common corner and form a filled

triangular Nb trimer with Se atoms at the center. That is, the Nb displacements of the two CDWs resemble two distortions of a single soft Nb breathing mode phonon, 180° out of phase. Different from the first phase, there are both in-plane and out-of-plane modulation for those six Se atoms on the hexagonal ring. As shown in Fig. 2(d), the modulation of those Se atoms not on the hexagonal ring pointing outward to the Nb layer vertically with no in-plane component. To confirm structural stability, the absence of soft modes in the phonon spectrum within the 2×2 BZ for both phases is illustrated in SM S.2..

The stability of these two phases is further supported by the local energy landscape when changing the trio of in-plane Nb (Nb trimer) distortions δ_{Nb} manually and fully relaxing all other atoms for each set of δ_{Nb} . The δ_{Nb} distortion set is chosen to obey the C_3 symmetry of the space group. The total energy per formula unit (f.u.) at different δ_{Nb} with lattice constants under 6% strain are shown in Fig. 2f. The energy has a local maximum at $\delta_{Nb} = 0$ (normal phase) and two inequivalent local minima at finite values of δ_{Nb} (phase 1 and phase 2), and the asymmetric double wells shape reflects the lack of inversion symmetry in monolayer $2H$ -NbSe₂. When cooling strained $2H$ -NbSe₂ through T_{CDW} , the system can settle into either configuration with no barrier. It takes at least around 20meV (~ 240 K) to overcome the barrier and transition to the other energy well corresponding to the other 2×2 phase. Therefore, even though one phase is around 8meV lower than the other one, we predict these two 2×2 phases will coexist in a strained monolayer $2H$ -NbSe₂ sample, possibly forming a long range landscape, as in the 3×3 phases [34], which could be verified by STM.

In Fig. 2g we compare the energies of the two 2×2 CDW phases, two 3×3 CDW phases [43, 44] (see SM S.3.) and the non-CDW phase. Fig. 2h shows the differences of total energy per f.u. relative to the energy of normal phase as a function of strain. It reveals that the 3×3 CDW phase 1 is the ground state with 0%-1% strain, but for higher strain the 2×2 CDW phase 2 becomes the ground state and both phases of 2×2 CDW have lower energies than the 3×3 CDW and normal phases. The strain-induced CDW phase transition from 3×3 to 2×2 phases is consistent with the shift of soft phonon modes in Fig. 1d and the inversion of energy hierarchy in Fig. 2g. Furthermore, the competition between 2×2 and 3×3 CDW phases around 1% strain also provides an explanation for their coexistence in the STM experiment. [39]

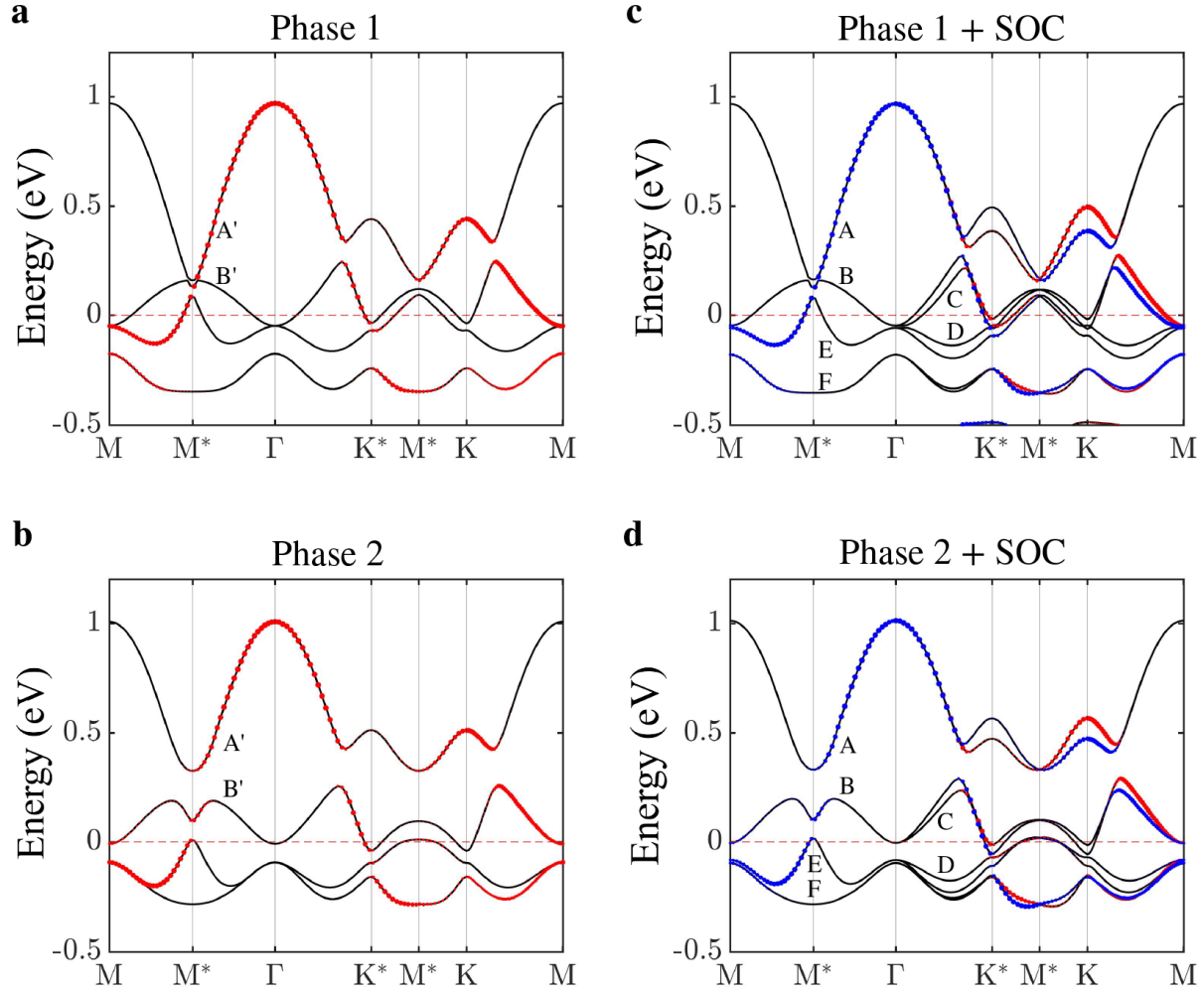


FIG. 3. **Band structure of both 2×2 CDW phases.** The folded and unfolded electronic band structure without/with SOC for **a/c** phase 1 and **b/d** phase 2 of 2×2 CDW. The folded bands are represented by the black curves. In **a** and **b**, the unfolded spectral weights are represented by the size of red markers. The two bands discussed in context is represented by band index A' and B'. In **c** and **d**, the unfolded spectral weights for spin up/down states are represented by the size of red/blue markers. Those bands discussed in context are represented by band index A-F.

ELECTRONIC BAND STRUCTURES

Fig. 3 shows the electronic band structures of the modulated phases under 6% in-plane biaxial tensile strain. The 2×2 CDW phases under different strain give rise to qualitatively similar electronic dispersions. The folded (black lines) and unfolded (markers) band structures without/with spin-orbit coupling (SOC) for phase 1 are shown in Fig. 3a/c. The

unfolded bands shown by the red and blue markers reveal how the CDW modifies the normal phase band structure in the 1×1 BZ (See SM S.4. for the normal phase band structure). Without SOC, the band dispersion around M^* along the Γ -M line displays a feature of band inversion between band A' and B' with the inverted gap $2\delta \sim 40\text{meV}$ as shown in Fig. 4a. As shown in Fig. 4b, two Dirac nodes appear near each M^* , which is a saddle point in the band structure hosting a Van Hove singularity, due to the crystalline mirror and time-reversal symmetries. Note that for both phases, all the bands on the Γ -M line are doubly-degenerate, which reflects the mirror line along the $\mathbf{b} - \mathbf{a}$ direction in the crystal structure as shown in Fig. 2a.

However, as shown in Fig. 4c, SOC opens a fundamental gap $E_g \sim 5\text{ meV}$ between bands A and B of phase 1 at around 0.15eV above the Fermi level. To check whether these two bands are connected away from the Γ -M line, the 2D energy dispersion in the zoomed-in region around M^* is shown in Fig. 4d. Bands A and B display a camelback shape near M^* , suggestive of band inversion with non-trivial band topology. From Fig. 4(c-d), it is clear that there is a full gap between bands A and B in the whole 2×2 BZ with fundamental gap $E_g \sim 5\text{ meV}$ and inverted gap $2\delta \sim 40\text{ meV}$.

To understand the origin of the inverted band structure near M^* , we analyze the orbital character of the bands and the results are shown by the size of markers in Fig. 4a, c. There is almost no d_{xz} and d_{yz} orbital character in the bands around the Fermi level which is consistent with orbital character in the normal phase. (See SM S.4.) From Fig. 4a, without including SOC, the structural distortion and the period doubling due to PLD cause the band inversion between d_{xy} and a combination of d_{z^2} and $d_{x^2-y^2}$ bands around M^* . Then, SOC opens the fundamental band gap between bands A and B in phase 1 without further band inversion as shown in Fig. 4c. It's worth emphasizing that SOC doesn't open a gap in the 2×2 normal phase (as shown in SM S.4.), thus the PLD due to 2×2 CDW phase transition is crucial in the formation of this gap.

Due to the existence of mirror symmetry M_z in the whole 2D BZ, we can separate all the bands by their mirror eigenvalues of M_z . For the phase 1 with SOC, there is a doubly-degenerate nodal ring around each K^* point, formed by bands C and D with opposite mirror eigenvalues as shown in Fig. 4(e-f). Note that, between these two bands, SOC opens a small fundamental gap at Γ and there is no other contact point besides the nodal rings.

Fig. 3b/d show the unfolded band structure without/with SOC of phase 2. Unlike the

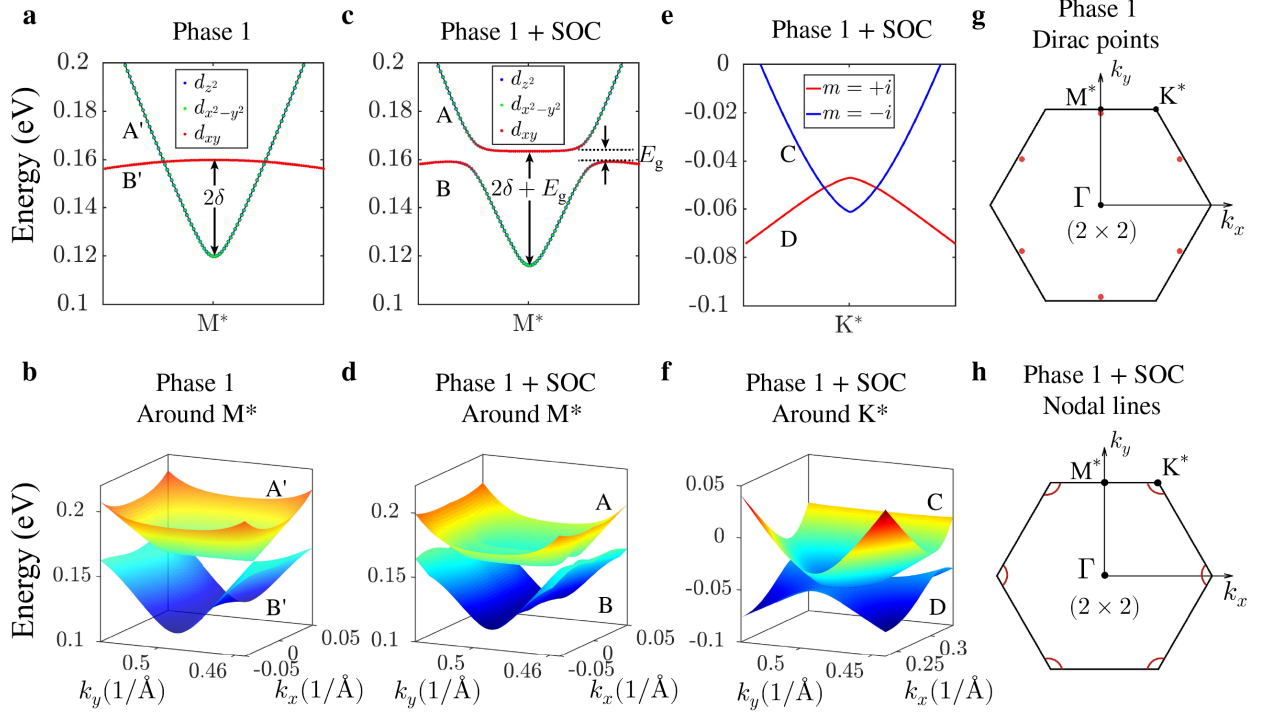


FIG. 4. **Topological band structure in 2×2 CDW phase 1.** (a-b) Energy dispersion of phase 1 without SOC between bands A' and B'. **a**, Along Γ -M* around the high symmetry point M*. 2δ , CDW inverted gap. For **a** and **c**, the dominant Nb d_{xy} , d_{z^2} and $d_{x^2-y^2}$ orbital weights are shown by the size of red, blue and green markers. **b**, The 2D region around M*. There are two Dirac points, one inside and another one outside the 2×2 BZ. (c-d) Energy dispersion including SOC between bands A and B around the high symmetry point M*. E_g , fundamental gap. **d**, A full gap is opened between band A and B even away from the high-symmetry line. (e-f) energy dispersion of phase 1 with SOC between bands C and D. **e**, Along the Γ -K* around the high symmetry point K*. The eigenvalues $m = +/ - i$ of the out-of-plane mirror symmetry M_z are represented by red/blue curves. **f**, The nodal ring around the K* between bands C and D in phase 1 with SOC. **g**, Red markers represent the positions of Dirac nodes composed by bands A' and B' of phase 1 without SOC in the 2×2 BZ. **h**, Red curves represent the positions of nodal rings composed by bands C and D of phase 1 with SOC in the 2×2 BZ.

band structure of phase 1, CDW opens a full gap between band A and band B even without including SOC. A band inversion feature of camelback shape near M* also appears in band B of phase 2. The orbital character is shown in Fig. 5a without SOC and Fig. 5b with SOC. We find that SOC plays negligible role in the band inversion around M* and the CDW has

already double inverted the d_{xy} bands. Instead, as shown in Fig. 3d, SOC opens a full CDW gap between bands E and F.

The band structure between bands E and F around Γ along $K^*-\Gamma-K^*$ is shown in Fig. 5c. Since the bands around the Fermi level are composed of Nb d_{xy} , d_{z^2} and $d_{x^2-y^2}$ orbitals which are all even under out-of-plane mirror M_z symmetry, so the M_z eigenvalues of these bands are consistent to the SOC induced spin splitting in the band structure. Therefore, the mirror eigenvalues of each spin-splitting pair are opposite to each other at two finite momentum \mathbf{k} and $-\mathbf{k}$ in the 2D BZ, and they exchange signs whenever they cross over the $\Gamma-M^*$ mirror lines which are spin-degenerate lines. The 2D dispersion of bands E and F is shown in Fig. 5d to demonstrate that there is no connected point even away from the high symmetry lines around Γ point. Besides, in contrast to phase 1, there are three full CDW gaps around the Fermi level in phase 2; There is an additional full CDW gap between bands C and D, and therefore there is no nodal ring in phase 2.

TOPOLOGY OF THE CDW PHASE

The band inversion induced by the CDW ordering indicates the possibility of non-trivial topology. Due to the existence of TRS and the full band gap between bands A and B within the folded BZ in both phases, the nature of its band topology within this CDW gap can be examined by calculating the TRS protected \mathbb{Z}_2 index. Because there is no inversion symmetry in the monolayer $2H$ structure, the \mathbb{Z}_2 index is calculated by the Wilson loop method [49] and we find that $\mathbb{Z}_2 = 1$ for phase 1 and $\mathbb{Z}_2 = 0$ for phase 2 as shown in Fig. 6(a-b), indicating that the phase 1 of 2×2 CDW hosts the QSH insulator phase in the CDW gap.

The analysis of orbital character provides an explanation for why the \mathbb{Z}_2 index is non-trivial for phase 1 but trivial for phase 2. For phase 1 in the absence of SOC, the band inversion due to CDW leads to the appearance of an inverted gap 2δ at M^* and six Dirac points near M^* in the 2×2 BZ as shown in Fig. 4g. SOC then opens up a fundamental gap $E_g \sim 5\text{meV}$ at these Dirac points leading to a QSH insulator. The schematic picture is shown in Fig. 5e. Since SOC cannot open the gap without the 2×2 CDW phase transition, the topology is purely induced from the CDW phase transition. However, for phase 2, band inversion due to the CDW has already opened a full gap without SOC, and the double band

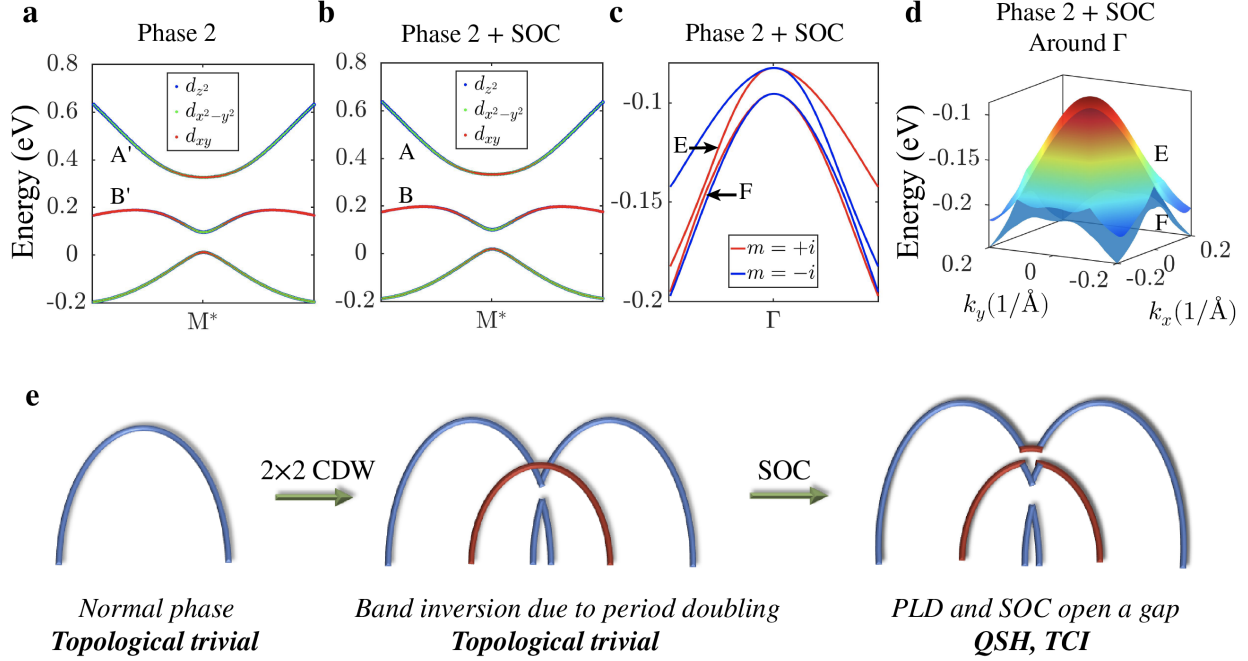


FIG. 5. **Band structure in 2×2 CDW phase 2 and the schematic picture on the formation of QSH state.** Energy dispersion around M^* along Γ - M^* - Γ line of phase 2. **a**, Without SOC **b**, with SOC. The dominant Nb d_{xy} , d_{z^2} and $d_{x^2-y^2}$ orbital weights are shown by the size of red, blue and green markers (**c-d**) Energy dispersion including SOC between band E and band F around the high symmetry point Γ . **c**, Band structure around Γ along K^* - Γ - K^* . The eigenvalues $m = +/ - i$ of the in-plane mirror symmetry M_z are represented by red/blue curves. **d**, The 2D region around Γ . A full gap is opened between band E and F even away from the high-symmetry line. **e**, Schematic picture on the formation of non-trivial topological state in 2×2 CDW phase. Note that the gap with band inversion is opened by the combination of SOC and 2×2 CDW phase transition. (See SM S.4. as a comparison)

inversion of d_{xy} bands at M^* leads to a trivial topology in phase 2.

The topology of nodal ring around K^* between bands C and D in phase 1, as shown in Fig 4(e-f), is confirmed by the zero-dimensional enclosing manifold [50]. By counting the number of occupied bands with M_z eigenvalue $m = i$ up to the energy of nodal ring at a point inside(outside) of the nodal ring denoted as $p_1(p_2)$, the \mathbb{Z} class topological invariance is defined as $\zeta_0 = N_{P_2,i} - N_{P_1,i} = 26 - 25 = 1$ which corresponding to a mirror-protected TNL semimetal.

We further examine the mirror Chern number for the full CDW gaps in both phases. The

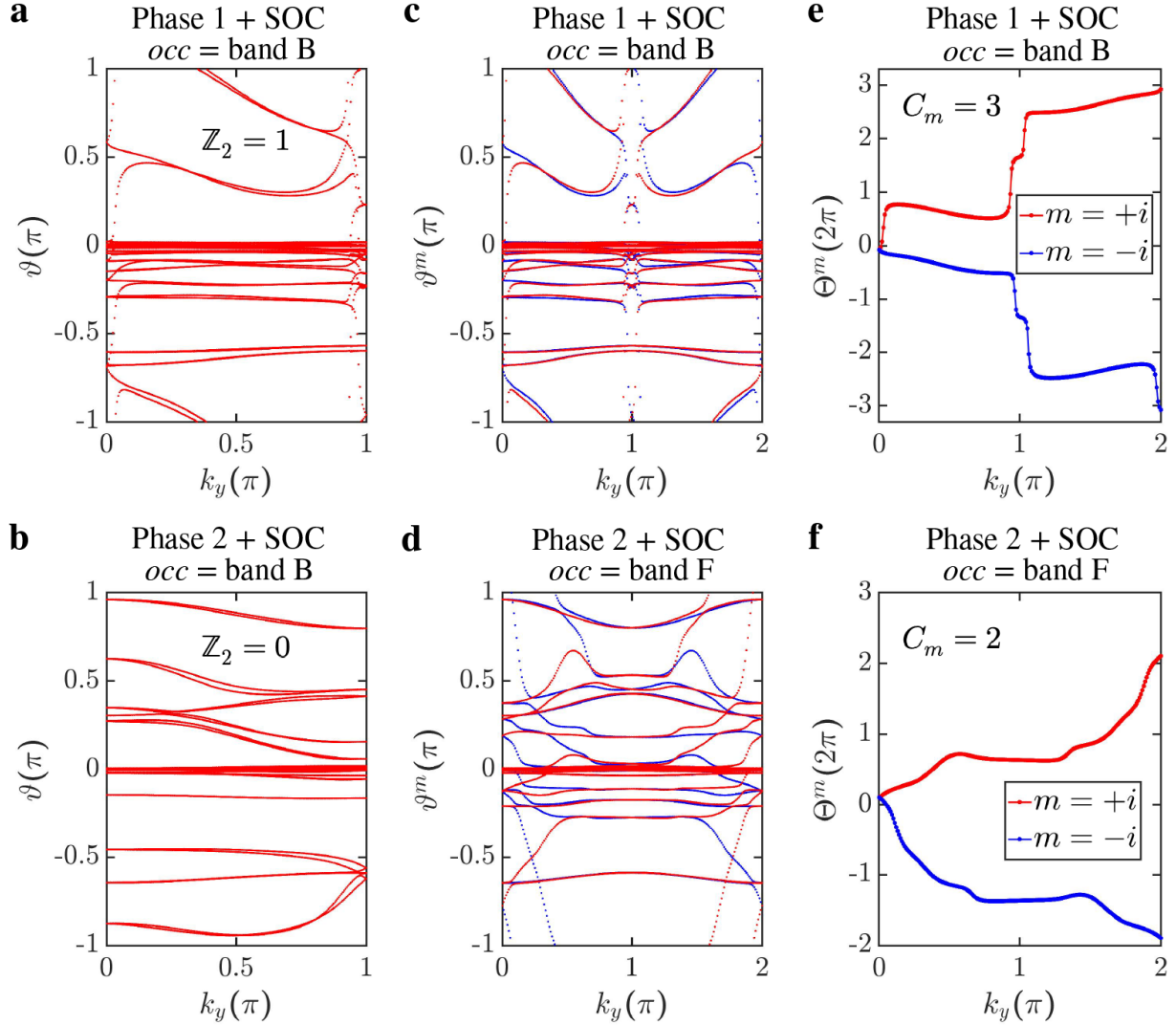


FIG. 6. **Wilson loop calculation on \mathbb{Z}_2 and mirror Chern number C_m .** (a-b) The Wannier charge center evolution along the principle axis k_y of the 2×2 BZ. The occupied bands are counted up to band B. **a**, Phase 1 with $\mathbb{Z}_2=1$. **b**, Phase 2 with $\mathbb{Z}_2=0$. (c-d) The Wannier charge center evolution with mirror eigenvalue separation along the principle axis k_y of the 2×2 BZ. For (c-f) the red/blue markers represent for mirror eigenvalue $m = +/ - i$. **c**, Phase 1 with occupied bands counted up to band B. **d**, Phase 2 with occupied bands counted up to band F. (e-f) The accumulated geometric phases Θ^m along k_y . **e**, $C_m=3$ for phase 1 with occupied band counted up to band B. **f**, $C_m=2$ for phase 2 with occupied band counted up to band F.

Wilson loop calculation with mirror eigenvalues $m = \pm i$ separation is shown in Fig. 6(c-d), and the accumulated geometric phase difference $\Theta^m \equiv \int \dot{\vartheta}_{k_y}^m dk_y$ along the principle axis k_y

is shown in Fig. 6(e-f), where $\dot{\vartheta}_{k_y}^m \equiv \sum_{n=1}^{occ} d\vartheta_{k_y,n}^m/dk_y$ with ϑ as the Berry phases, n as the band index and occ as the number of occupied bands. Since the first Chern class of the sub Hilbert space with each mirror eigenvalue m is identified as $C_{\pm i} = \Theta^{\pm i}/2\pi$, we find the mirror Chern number $C_m = \frac{1}{2}(C_{+i} - C_{-i}) = 3$ for phase 1 when the occupied bands are counted up to band B, and $C_m = 2$ for phase 2 when the occupied bands are counted up to band F, indicating that both phases of 2×2 CDW coexist with the topological crystalline insulator (TCI) state. It is worth emphasizing that the 2×2 CDW phase 1 is a triple-topological state where both QSH and TCI states coexist in the a full CDW gap between bands A and B, and the mirror-protected topological nodal rings occur between bands C and D.

CONCLUSION

Our first-principles modeling and analysis show that the 2×2 CDW phase of monolayer $2H$ -NbSe₂ could assume two stable crystal structures. The phonon spectrum and energy hierarchy from our DFT calculations explain the coexistence of 3×3 and 2×2 triangular phases seen in experiments [39]. As a function of strain, both the shifting of the soft phonon mode and the inversion in energy hierarchy support the strain-induced CDW phase to transition from the 3×3 triangular phase to the 2×2 triangular phase. Since both of the two 2×2 phases are equally preferred prior to spontaneous symmetry-breaking, we predict the coexistence of these two phases in a strained monolayer of $2H$ -NbSe₂, which could be verified by further STM experiments.

We also predict both the 2×2 CDW phases we have identified to be topological. The 2×2 CDW Phase 1 is a triple-topological CDW phase encompassing a QSH insulator, TCI and TNL semimetal states. In contrast, the 2×2 CDW Phase 2 only contain the TCI state. This is the first prediction of the TCI and TNL states coexisting with a CDW. Since the unmodulated phase here is trivial, the topological phases emerge directly from the formation of charge order in the CDW. Combining our finding of the three emergent topological states, the new competing CDW phases, and the coexistence of a superconducting state [35] suggests that monolayer $2H$ -NbSe₂ could provide an exciting sandbox for exploring the interplay between correlation effects and topological states. It could also provide a unique materials platform for developing applications in quantum electronics and spintronics, and Majorana-based topological quantum computing.

ACKNOWLEDGMENTS

We thank Chao-Sheng Lian, for providing their 3×3 CDW structures in [43]. The work at Northeastern University was supported by the US Department of Energy (DOE), Office of Science, Basic Energy Sciences Grant No. DE-SC0019275 (materials discovery for QIS applications) and benefited from Northeastern University’s Advanced Scientific Computation Center and the National Energy Research Scientific Computing Center through DOE Grant No. DE-AC02-05CH11231. H.L. acknowledges the support by the Ministry of Science and Technology (MOST) in Taiwan under grant number MOST 109-2112-M-001-014-MY3. S.M. and A.A. gratefully acknowledge the HPC facility at Indian Institute of Technology Kanpur, for computational resources. J.N. benefited from resources of the Tampere Center for Scientific Computing, TCSC. T.H.’s research is supported by the ITU-BAP project TDK-2018-41181. T.-R.C. was supported by the Young Scholar Fellowship Program from the Ministry of Science and Technology (MOST) in Taiwan, under a MOST grant for the Columbus Program MOST110-2636-M-006-016, NCKU, Taiwan, and National Center for Theoretical Sciences, Taiwan. Work at NCKU was supported by the MOST, Taiwan, under grant MOST107-2627-E-006-001 and Higher Education Sprout Project, Ministry of Education to the Headquarters of University Advancement at NCKU.

METHODOLOGY

The lattice dynamics calculations of the unmodulated 1×1 structure were carried out within the framework of density functional perturbation theory (DFPT) [51] using norm-conserving pseudo-potentials [52] as implemented in the Quantum Espresso simulation package [53]. The exchange-correlation effects are treated within the local density approximation (LDA) [54] with the Perdew-Zunger parametrization [55]. We have fully optimized both the ionic positions and lattice parameters until the residual forces on each ion were less than 10^{-4} Ry and zero-stress tensors are obtained. The monolayer is obtained from the relaxed bulk structure by setting a vacuum of 14 \AA along the z-direction to eliminate the interaction with spurious replica images. Another ionic relaxation for monolayer structure follows this to ensure structural stability. The in-plane biaxial tensile strain is simulated by increasing the lattice parameter based on the relaxed monolayer structure. For the strained 1×1

structure, we only relax the atoms position by fixing the lattice parameter and unit cell shape. For normal phase, the phonon dispersion is obtained by Fourier interpolation of the dynamical matrices computed on a $24 \times 24 \times 1$ k -mesh and $12 \times 12 \times 1$ q -mesh [6]. For the 2×2 CDW phase, the Brillouin zones for electronic and vibrational calculations are sampled using $9 \times 9 \times 1$ and $2 \times 2 \times 1$ respectively.

The lattice relaxation of the modulated structures and all of the electronic structure calculations were carried out within the DFT framework with the projector augmented wave (PAW) method using the Vienna *ab initio* Simulation Package (VASP) [54, 56–59]. We used the strongly-constrained-and-appropriately-normed (SCAN) meta-generalized-gradient-approximation (meta-GGA) energy functionals with the Perdew-Burke-Ernzerhof (PBE) parametrization [60] to include exchange-correlation effects in computations. An energy cut-off of 400 eV was used for the plane-wave-basis set. To keep approximately same distance between the sampling k -points, the Γ -centered $21 \times 21 \times 1$, $11 \times 11 \times 1$ and $7 \times 7 \times 1$ k -mesh was employed accordingly to sample the 2D Brillouin zone (BZ) of 1×1 , 2×2 and 3×3 monolayer structure. The ionic relaxation of modulated 2×2 and 3×3 structures is set to converge upon satisfying the condition of residual forces smaller than 10^{-3} eV \AA^{-1} per atom and energy tolerance smaller than 10^{-4} eV per unit cell. The first order Methfessel-Paxton smearing method with smearing width 0.1 eV was used in the ionic relaxation process, the tetrahedron method with smearing width 0.1 eV was used in the self-consistent run of electronic structure, and the Gaussian smearing with smearing width 0.1 eV was used to calculate the electronic band structure along high-symmetry line. The spin-orbit coupling (SOC) is not included in the ionic relaxation process, and the SOC effects are included self-consistently in the electronic structure calculations. The topological analysis was performed by employing a real-space tight-binding model Hamiltonian, which was obtained by using the VASP2WANNIER90 interface [61]. Nb d and Se p states were included in generating Wannier functions. All crystal structures are visualized using the VESTA [62] package.

AUTHOR CONTRIBUTIONS

W.C.C., S.M., R.M., J.N., B.S., T.H., H.L. and A.B. initiated the project. W.C.C and S.M. performed first-principles calculations and theoretical analysis with guidance from

R.M., J.N., B.S., T.H., A.A., T.R.C., H.L. and A.B.. All authors discussed the results and contributed to the planning and writing the manuscript.

COMPETING FINANCIAL INTERESTS

The authors declare no competing financial interests.

* chiu.w@northeastern.edu

† ar.bansil@northeastern.edu

- [1] Wen, X.-G. Choreographed entanglement dances: Topological states of quantum matter. *Science* **363**, eaal3099 (2019).
- [2] Raghu, S., Qi, X.-L., Honerkamp, C. & Zhang, S.-C. Topological mott insulators. *Phys. Rev. Lett.* **100**, 156401 (2008).
- [3] Shi, W. et al. A charge-density-wave topological semimetal. *Nature Physics* (2021).
- [4] Mitsuishi, N. et al. Switching of band inversion and topological surface states by charge density wave. *Nature Communications* **11**, 2466 (2020).
- [5] Jiang, Y.-X. et al. Discovery of topological charge order in kagome superconductor KV_3Sb_5 (2020). [arXiv:2012.15709](https://arxiv.org/abs/2012.15709).
- [6] Correa, L. E. et al. Multiband superconductivity and charge density waves in the topological semimetal ni-doped $ZrTe_2$ (2021). [arXiv:2102.04812](https://arxiv.org/abs/2102.04812).
- [7] Kane, C. L. & Mele, E. J. Z_2 topological order and the quantum spin hall effect. *Phys. Rev. Lett.* **95**, 146802 (2005).
- [8] Kane, C. L. & Mele, E. J. Quantum spin hall effect in graphene. *Phys. Rev. Lett.* **95**, 226801 (2005).
- [9] Bernevig, B. A. & Zhang, S.-C. Quantum spin hall effect. *Phys. Rev. Lett.* **96**, 106802 (2006).
- [10] Liu, J. et al. Spin-filtered edge states with an electrically tunable gap in a two-dimensional topological crystalline insulator. *Nature Materials* **13**, 178–183 (2014).
- [11] Wrasse, E. O. & Schmidt, T. M. Prediction of two-dimensional topological crystalline insulator in PbSe monolayer. *Nano Letters* **14**, 5717–5720 (2014).

- [12] Jin, Y.-J. et al. The prediction of a family group of two-dimensional node-line semimetals. *Nanoscale* **9**, 13112–13118 (2017).
- [13] Jin, L. et al. Two-dimensional weyl nodal-line semimetal in a d^0 ferromagnetic K_2N monolayer with a high curie temperature. *Phys. Rev. B* **102**, 125118 (2020).
- [14] Niu, C. et al. Robust dual topological character with spin-valley polarization in a monolayer of the dirac semimetal Na_3Bi . *Phys. Rev. B* **95**, 075404 (2017).
- [15] Bernevig, B. A., Hughes, T. L. & Zhang, S.-C. Quantum spin hall effect and topological phase transition in $HgTe$ quantum wells. *Science* **314**, 1757 (2006).
- [16] König, M. et al. Quantum spin hall insulator state in $HgTe$ quantum wells. *Science* **318**, 766 (2007).
- [17] Qian, X., Liu, J., Fu, L. & Li, J. Quantum spin hall effect in two-dimensional transition metal dichalcogenides. *Science* **346**, 1344–1347 (2014).
- [18] Tang, S. et al. Quantum spin hall state in monolayer $1T'-WTe_2$. *Nature Physics* **13**, 683–687 (2017).
- [19] Fei, Z. et al. Edge conduction in monolayer WTe_2 . *Nature Physics* **13**, 677–682 (2017).
- [20] Leroux, M. et al. Strong anharmonicity induces quantum melting of charge density wave in $2H - NbSe_2$ under pressure. *Phys. Rev. B* **92**, 140303 (2015).
- [21] Flicker, F. & van Wezel, J. Charge order from orbital-dependent coupling evidenced by $NbSe_2$. *Nature Communications* **6**, 7034 (2015).
- [22] Zhu, X. et al. Signature of coexistence of superconductivity and ferromagnetism in two-dimensional $NbSe_2$ triggered by surface molecular adsorption. *Nature Communications* **7**, 11210 (2016).
- [23] Manzeli, S., Ovchinnikov, D., Pasquier, D., Yazyev, O. V. & Kis, A. 2D transition metal dichalcogenides. *Nature Reviews Materials* **2**, 17033 (2017).
- [24] Roldán, R., Castellanos-Gomez, A., Cappelluti, E. & Guinea, F. Strain engineering in semiconducting two-dimensional crystals. *Journal of Physics: Condensed Matter* **27**, 313201 (2015).
- [25] Shi, Y. et al. Imaging quantum spin hall edges in monolayer WTe_2 . *Science Advances* **5**, eaat8799 (2019).
- [26] Zhou, Y. et al. Tensile strain switched ferromagnetism in layered NbS_2 and $NbSe_2$. *ACS Nano* **6**, 9727–9736 (2012).

- [27] Xu, Y., Liu, X. & Guo, W. Tensile strain induced switching of magnetic states in NbSe₂ and NbS₂ single layers. *Nanoscale* **6**, 12929–12933 (2014).
- [28] Zheng, F., Zhou, Z., Liu, X. & Feng, J. First-principles study of charge and magnetic ordering in monolayer NbSe₂. *Phys. Rev. B* **97**, 081101 (2018).
- [29] Singh, B., Hsu, C.-H., Tsai, W.-F., Pereira, V. M. & Lin, H. Stable charge density wave phase in a 1T-TiSe₂ monolayer. *Phys. Rev. B* **95**, 245136 (2017).
- [30] Revolinsky, E., Spiering, G. & Beerntsen, D. Superconductivity in the niobium-selenium system. *Journal of Physics and Chemistry of Solids* **26**, 1029–1034 (1965).
- [31] Moncton, D. E., Axe, J. D. & DiSalvo, F. J. Study of superlattice formation in 2H-NbSe₂ and 2H-TaSe₂ by neutron scattering. *Phys. Rev. Lett.* **34**, 734–737 (1975).
- [32] Calandra, M., Mazin, I. I. & Mauri, F. Effect of dimensionality on the charge-density wave in few-layer 2H-NbSe₂. *Phys. Rev. B* **80**, 241108 (2009).
- [33] Xi, X. et al. Strongly enhanced charge-density-wave order in monolayer NbSe₂. *Nature Nanotechnology* **10**, 765–769 (2015).
- [34] Gye, G., Oh, E. & Yeom, H. W. Topological landscape of competing charge density waves in 2H-NbSe₂. *Phys. Rev. Lett.* **122**, 016403 (2019).
- [35] Ugeda, M. M. et al. Characterization of collective ground states in single-layer NbSe₂. *Nature Physics* **12**, 92–97 (2016).
- [36] Wang, H. et al. High-quality monolayer superconductor nbse2 grown by chemical vapour deposition. *Nature Communications* **8**, 394 (2017).
- [37] Xi, X. et al. Ising pairing in superconducting nbse 2 atomic layers. *Nature Physics* **12**, 139–143 (2016).
- [38] Wickramaratne, D., Khmelevskiy, S., Agterberg, D. F. & Mazin, I. I. Ising superconductivity and magnetism in nbse₂. *Phys. Rev. X* **10**, 041003 (2020).
- [39] Gao, S. et al. Atomic-scale strain manipulation of a charge density wave. *Proceedings of the National Academy of Sciences* **115**, 6986 (2018).
- [40] Soumyanarayanan, A. et al. Quantum phase transition from triangular to stripe charge order in nbse₂. *Proceedings of the National Academy of Sciences* **110**, 1623–1627 (2013).
- [41] Leriche, R. T. et al. Misfit layer compounds: A platform for heavily doped 2d transition metal dichalcogenides. *Advanced Functional Materials* **31**, 2007706 (2021).

- [42] Silva-Guillén, J. Á., Ordejón, P., Guinea, F. & Canadell, E. Electronic structure of $2H$ -NbSe₂ single-layers in the CDW state. *2D Materials* **3**, 035028 (2016).
- [43] Lian, C.-S., Si, C. & Duan, W. Unveiling charge-density wave, superconductivity, and their competitive nature in two-dimensional nbse2. *Nano Letters* **18**, 2924–2929 (2018).
- [44] Guster, B. et al. Coexistence of elastic modulations in the charge density wave state of $2H$ -NbSe₂. *Nano Letters* **19**, 3027–3032 (2019).
- [45] Cossu, F., Palotás, K., Sarkar, S., Di Marco, I. & Akbari, A. Strain-induced stripe phase in charge-ordered single layer NbSe₂. *NPG Asia Materials* **12**, 24 (2020).
- [46] El-Bana, M. S. et al. Superconductivity in two-dimensional NbSe₂ field effect transistors. *Superconductor Science and Technology* **26**, 125020 (2013).
- [47] Weber, F. et al. Extended phonon collapse and the origin of the charge-density wave in $2H$ -NbSe₂. *Phys. Rev. Lett.* **107**, 107403 (2011).
- [48] McMillan, W. L. Microscopic model of charge-density waves in $2H$ - TaSe₂. *Phys. Rev. B* **16**, 643–650 (1977).
- [49] Soluyanov, A. A. & Vanderbilt, D. Computing topological invariants without inversion symmetry. *Phys. Rev. B* **83**, 235401 (2011).
- [50] Fang, C., Weng, H., Dai, X. & Fang, Z. Topological nodal line semimetals. *Chinese Physics B* **25**, 117106 (2016).
- [51] Baroni, S., Giannozzi, P. & Testa, A. Green’s-function approach to linear response in solids. *Phys. Rev. Lett.* **58**, 1861–1864 (1987).
- [52] Troullier, N. & Martins, J. L. Efficient pseudopotentials for plane-wave calculations. *Phys. Rev. B* **43**, 1993–2006 (1991).
- [53] Giannozzi, P. et al. QUANTUM ESPRESSO: a modular and open-source software project for quantum simulations of materials. *Journal of Physics: Condensed Matter* **21**, 395502 (2009).
- [54] Kohn, W. & Sham, L. J. Self-consistent equations including exchange and correlation effects. *Phys. Rev.* **140**, A1133–A1138 (1965).
- [55] Perdew, J. P. & Zunger, A. Self-interaction correction to density-functional approximations for many-electron systems. *Phys. Rev. B* **23**, 5048–5079 (1981).
- [56] Kresse, G. & Joubert, D. From ultrasoft pseudopotentials to the projector augmented-wave method. *Phys. Rev. B* **59**, 1758–1775 (1999).
- [57] Hohenberg, P. & Kohn, W. Inhomogeneous electron gas. *Phys. Rev.* **136**, B864–B871 (1964).

- [58] Kresse, G. & Furthmüller, J. Efficient iterative schemes for ab initio total-energy calculations using a plane-wave basis set. *Phys. Rev. B* **54**, 11169–11186 (1996).
- [59] Perdew, J. P., Burke, K. & Ernzerhof, M. Generalized gradient approximation made simple. *Phys. Rev. Lett.* **77**, 3865–3868 (1996).
- [60] Sun, J., Ruzsinszky, A. & Perdew, J. P. Strongly constrained and appropriately normed semilocal density functional. *Phys. Rev. Lett.* **115**, 036402 (2015).
- [61] Marzari, N. & Vanderbilt, D. Maximally localized generalized wannier functions for composite energy bands. *Phys. Rev. B* **56**, 12847–12865 (1997).
- [62] Momma, K. & Izumi, F. *VESTA3* for three-dimensional visualization of crystal, volumetric and morphology data. *Journal of Applied Crystallography* **44**, 1272–1276 (2011).

Supplementary Material: Topological charge density wave in monolayer NbSe₂

S.1. THE PHONON SPECTRUM FOR UNMODULATED STRUCTURE.

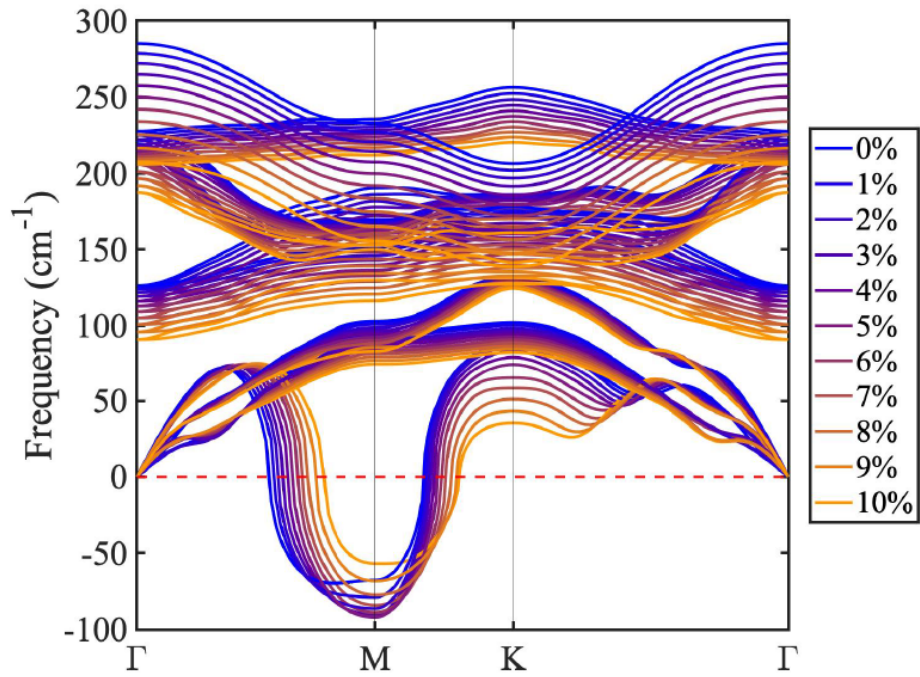


FIG. 7. **The phonon spectrum for unmodulated structure.** Phonon spectrum for the normal unmodulated phase under 0% to 10% strain.

S.2. THE 2×2 CDW PHONON SPECTRUM.

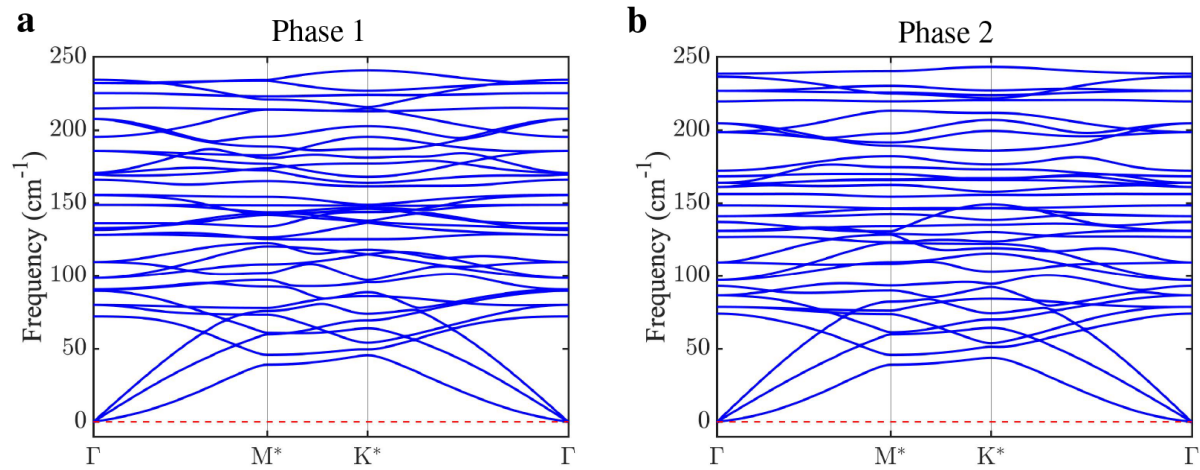


FIG. 8. **The 2×2 CDW phonon spectrum.** **a.** phase 1. **b.** phase 2. The stability of these two phases are reflected by the absence of soft phonon modes.

S.3. 3×3 CDW CRYSTAL STRUCTURE OF MONOLAYER $2H\text{-NbSe}_2$.

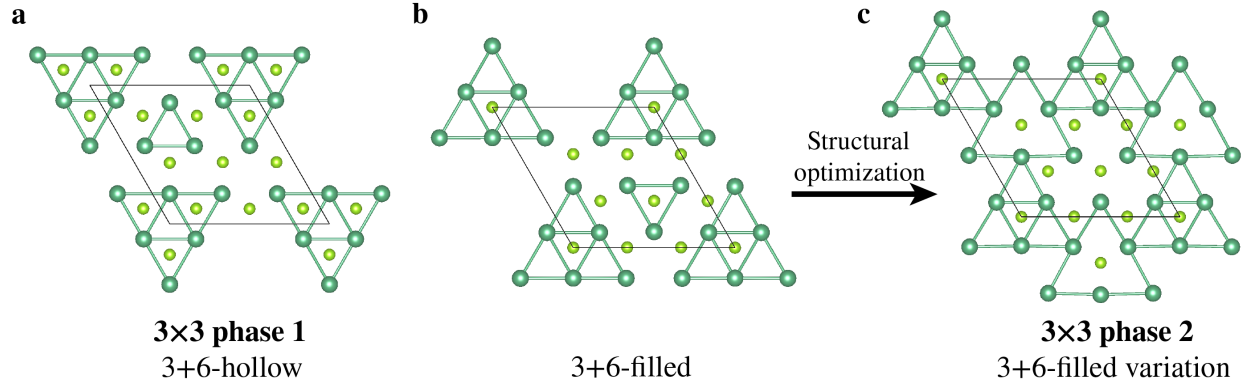


FIG. 9. 3×3 CDW crystal structure. (a-c). Nb and Se atoms are shown as dark green and light green spheres. The green lines represent the length of adjacent Nb-Nb atoms get shortened in the CDW phase. **a.** 3×3 phase 1. It can be referred as the “3+6-hollow” structure in Ref. [43]. **b.** “3+6-filled” structure in Ref. [43]. The structures in (a-b) are provided by Chao-Sheng Lian. **c.** 3×3 phase 2. In our calculation, the “3+6-filled” structure is not stable under structural optimization and it becomes a variation of “3+6-filled” structure. It is referred as the “Triangles 2” structure in Ref. [44].

S.4. 2×2 NORMAL PHASE BAND STRUCTURE.

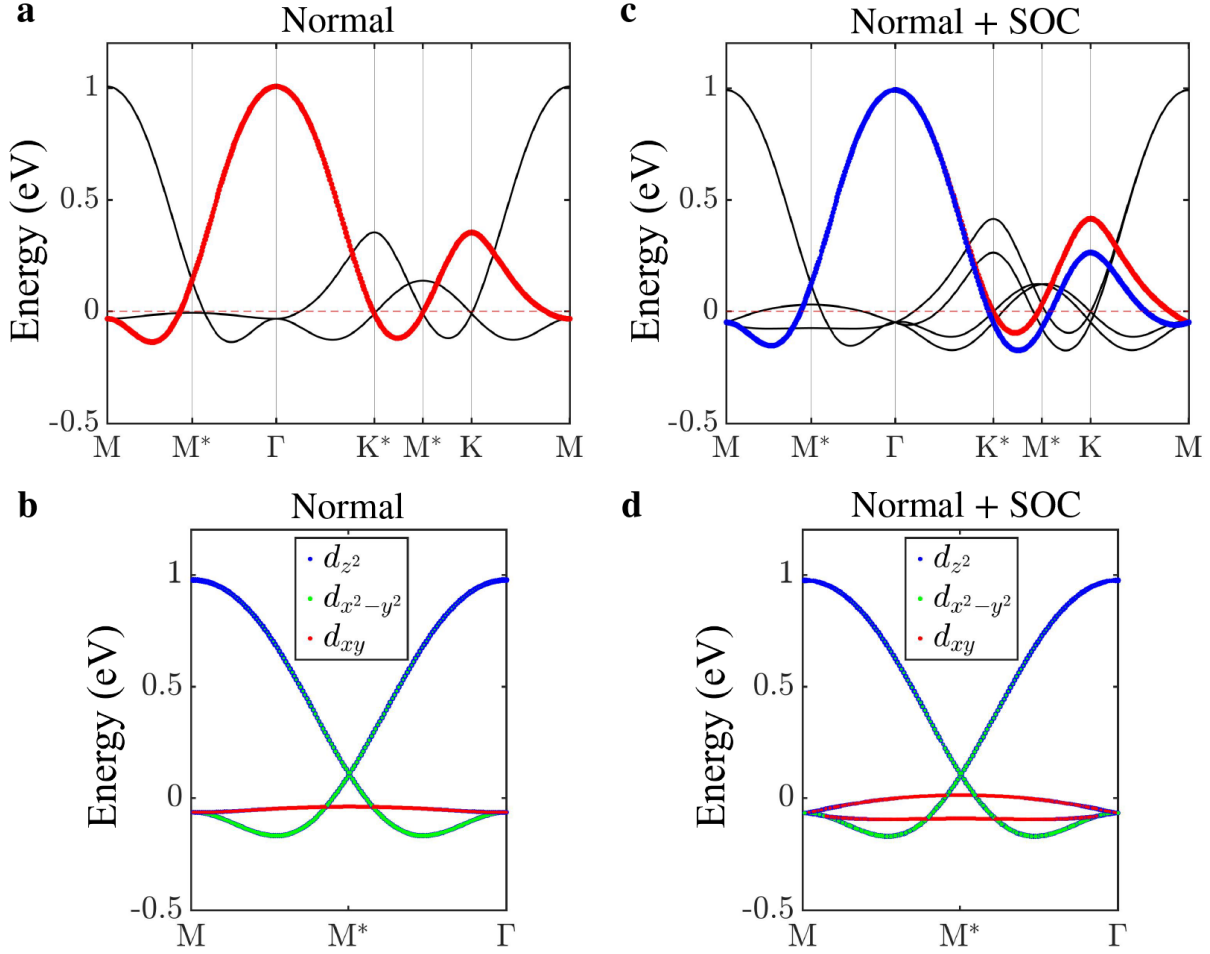


FIG. 10. 2×2 normal phase band structure. The folded and unfolded electronic band structure of 2×2 normal phase under 6% in-plane biaxial strain. (a-b), Without SOC. (c-d), With SOC. The folded bands are represented by the black curves. In a, the unfolded spectral weights are represented by the size of red markers. In c, the unfolded spectral weights for spin up/down states are represented by the size of red/blue markers. The unfolded spectral weights reveal the normal phase band structure in 1×1 BZ. For b and d, energy dispersion along M-M*- Γ . The dominant Nb d_{xy} , d_{z^2} and $d_{x^2-y^2}$ orbital weights are shown by the size of red, blue and green markers. In contrast to the CDW phase, there is no gap opened by the SOC in the normal phase, so it reveals that the QSH insulator and the TCI states are induced by the CDW.